Investigating the Performance of a Variable Stiffness Magnetic Spring for Resonant Ocean Power Generation

Md Emrad Hossain, Student Member, IEEE
Department of Electrical and Computer Engineering
Portland State University, Portland, OR, 97201, USA
mdemrad@pdx.edu

Jonathan Z. Bird, Member, IEEE
Department of Electrical and Computer Engineering
Portland State University, Portland, OR, 97201, USA
jonathan.bird@ieee.org

***Abstract* — This paper presents a new type of variable stiffness magnetic spring which can have a highly linear translational force characteristic. The variable stiffness is achieved through the rotation of a central magnet. Both positive and negative spring constants can be created. Using an analytic-based field analysis modelling technique the operating principle and linearity characteristics of the adjustable magnetic spring are studied. The use of a magnetic spring with an adjustable negative spring constant could enable an ocean generator to continuously operate in a resonant state thereby greatly increasing its power generation capability. The presented variable stiffness spring could also be useful in other energy harvesting and robotic actuator applications.**

Keywords— Analytical method, electromagnetic force, finite element analysis, magnetization, permanent magnet, springs.

I. Introduction

The coupling of a wave energy converter (WEC) with the generator system can be represented as a mass-spring-damper system [1-3]. An electrical analogy is shown in Fig. 1. In order for the WEC to be at resonance, and therefore maximize ocean power extraction, the generator and WEC damping term must be equal such that $B_g(t) = B_w(t)$. And the stiffness and mass must be related to the wave's forcing frequency, ω_o by [3]

$$\omega_o(t) = \sqrt{\frac{K_w(t) + K_g(t)}{m}} \tag{1}$$

As wave motion is slow the resonance frequency, ω_o, is always very small. Therefore, in order for the WEC to be at resonance either the WEC mass, m, has to be very large or the total system's spring constant term on the numerator of (1) must be small. If the generator spring constant, $K_g(t)$, can be actively controlled to have a varying negative value then the generators reactance could be lowered and made to match the WEC reactance, the WEC could then be made to operate continuously at resonance [3]. One approach to making the generator operate with a negative spring constant is to use a direct-drive generator with active current control. The direct-drive generator can be controlled to provide the generator forces that mimic a negative spring constant. Such an approach was studied in [3, 4]. It was shown that the generators voltage and current are respectively related to the damping and stiffness terms. Therefore, in order to provide both a sizable generator damping as well as negative stiffness the generator voltage and current must be highly out of phase and thus an extremely large amount of reactive power must be created by the generator. This vastly increases the WECs generator and power converter cost [3] making such a control approach cost-prohibitive.

Another option is to use a mechanical spring with a negative spring constant [5] in conjunction with a generator this decouples the negative spring control from the generator. The generator then only provides the WEC damping [2]. For instance, *CorPower Ocean AB* is using a set of three symmetrically separated mechanical springs to create an adjustable negative spring constant [5]. *CorPower* has stated that using a negative spring constant, can result in a six times increase in power output relative to a detuned WEC [5], other authors have stated similar levels of WEC power output improvements when using reactive control with a negative spring constant [1].

The currently developed adjustable stiffness mechanical springs are highly complex devices with many parts [5-8]. In order to reduce their complexity, improve efficiency and reliability a number of different variable stiffness magnetic actuators have been studied for use in resonant generators and robotic applications [9-12]. A magnetic spring force can be created by using two vertical opposing polarity magnets [13-20] or horizontally positioned magnets [14, 20-25]. However, the force between the magnets is often highly nonlinear and the decreases rapidly with separation distance. Therefore, using such a magnetic spring makes it challenging to control and limits the force capability and translational length of the

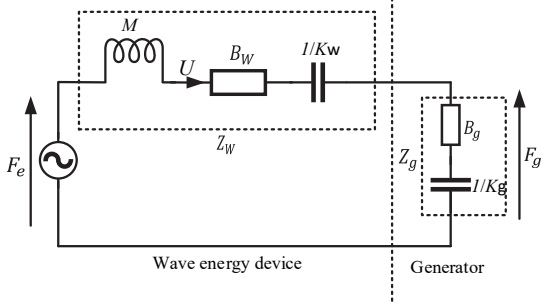

Fig. 1. An electrical analogue of a wave energy device (buoy) and power take-off generator [3]

spring [12]. A linearity relationship can often be achieve close to the equilibrium but only for a relatively small displacement [9].

A number of authors have investigated the performance of a negative magnetic springs, for instance in [26, 27] it was studied for structural vibration isolation. In almost all such magnetic spring designs the stiffness cannot be changed. One exception is in [10] in which the authors have demonstrated a way in which a rotary magnetic torsion spring can have an adjustable spring constant by axially shifting the rotors. However, in this design the magnetic spring stiffness is still nonlinear.

The focus of this paper is to investigate the performance capabilities of a new type of variable stiffness magnetic spring for a WEC application that has an adjustable stiffness as well as high force density.

II. An Adjustable Magnetic Spring

The configuration of the proof-of-principle adjustable magnetic spring is shown in Fig. 2 it consists of four Nd-Fe-B permanent magnets. The two rectangular cuboidal side magnets are mechanically allowed to move only translationally along the *z*-axis, and they are magnetized in opposite directions along the *z*-axis as shown. The two cylindrical tube magnets are magnetized diametrically and allowed to rotate only around the *z*-axis. An *x*-*y* axis field plot showing the field lines for all the magnets is shown in Fig. 3 for the case when the cuboidal magnets are vertically offset at a rotor angle positions of $\theta_k = 0^o$ and $\theta_k = 180^o$. When the magnets are centered at $\theta_k = 0^o$, as shown in Fig. 3(a), the field lines circulate around through all the magnets providing a positive stiffness whereas when the central tube magnets are rotated to $\theta_k = 180^o$ the cylinder tube magnets are fully opposing the cuboidal magnets a negative spring stiffness value is created. The cylinder tube magnets can be rotated around between these two extremes yielding a continuous range of spring stiffness values. When a stepper motor with brake is utilized then the stiffness can be adjusted and held fixed without then expending power to maintain the spring stiffness value, as would be the case if a linear motor was used to create the linear force.

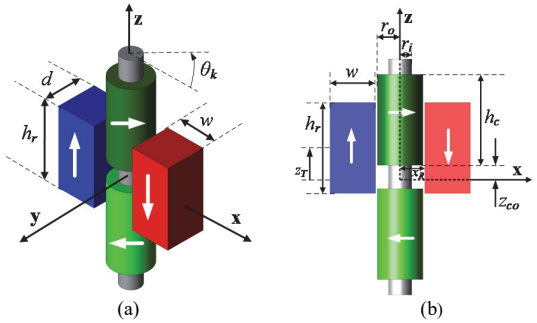

(a) (b)

Fig. 2. (a) Perspective view and (b) plan view of the adjustable magnetic spring composed of two cuboidal magnets and two diametric cylindrical tube magnets. The cuboidal magnets can translationally move along the *z*-axis and the tube magnets can rotate around the *z*-axis. An angle offset $\theta_k = 30^o$ from the zero torque position is shown in the figure. [28]

III. Sizing Analysis

The geometric values for the proof-of-principle adjustable magnetic spring are shown in Table I. The air-gap space between the cylindrical tube magnet and rectangular cuboidal magnet is $g = 0.5$mm and the Nd-Fe-B magnet grade is N50. Fig. 4 and Fig. 5 show both the force and torque created by the magnetic spring as a function of both rotation angle, θ_k, and translational displacement, z_t. It can be seen that whilst the force is linear between the stroke length of $z_T = \pm 10$ mm the force is not fully linear up to the peak force. In order to study the force relationship and improve the stroke length characteristics a 3-D analytic-based model was recently developed [28]. In this model the magnetics field was computed using magnetic charge functions and then the force was computed using the magnetic energy, *U*. For instance, the torque as a function of translational displacement, z_T, and rotation angle, θ_k, can be computed using [29]

$$T_z(\theta_k, z_T) = \left.\frac{\partial U(\theta_k, z_T)}{\partial \theta_c}\right|_{\phi_r = \text{constant}} \tag{2}$$

where ϕ_r = magnetic scalar potential. The force can be evaluated from [29]

$$F_z(z_T, \theta_k) = -\left.\frac{\partial U(z_T, \theta_k)}{\partial z}\right|_{\sigma_c = \text{constant}} \tag{3}$$

where σ_c = magnetic charge function. Using the force and torque analytic equations Fig. 4 and Fig. 5 shows that a good match with the finite element analysis (FEA) simulated model was achieved [28].

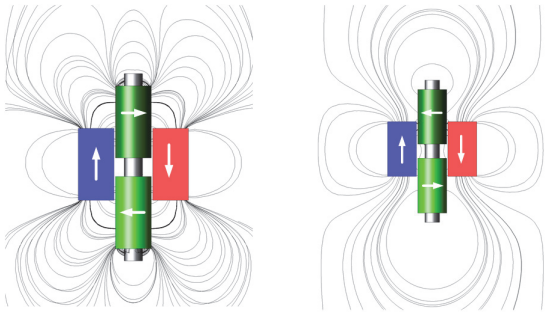

(a) (b)

Fig. 3.(a) Magnetic vector potential contour lines around the magnetic spring at (a) (θ_k, z_T) = (0°, 2 mm) and (b) at an angle of (θ_k, z_T) = (180°, 2 mm).

Utilizing the analytic force-torque model [28] a parametric sweep analysis was conducted. The following parameter relationships were investigated:

A. Cylindrical magnet separation length
B. Magnet height ratio
C. Height-to-width ratio
D. Cuboidal depth-to-width ratio
E. Cylindrical tube diameter-to-width ratio

The objective of the analysis was to gain a better intuitive understand of the force relationships whilst also trying to maximize the force density. The force density is defined as

$$F_d = \frac{\max(F_z(0, z_T))}{2[wdh_r + \pi(r_o^2 - r_i^2)h_c]\rho_m} \tag{4}$$

where $\rho_m = 7500$ kg/m^3 magnet density. The peak force at $\theta_k = 0^o$ was used to compute the force density. For analysis clarity the force plot and peak force in this section are only shown for the postive force-displacement region.

TABLE I
ADJUSTABLE MAGNETIC SPRING PARAMETERS

Description		Value	Units
Rectangular cuboidal magnets	Height, h_r	25	mm
	Width, w	12.5	mm
	Depth, d	12.5	mm
	Lateral offset, x_R	6.75	mm
Diametric cylindrical tube magnet	Height, h_c	25	mm
	Inner radius, r_i	3.175	mm
	Outer radius, r_o	6.25	mm
	Axial separation gap from center, z_{co}	3.25	mm
Air-gap between cylinder and cuboidal magnet, g		0.5	mm

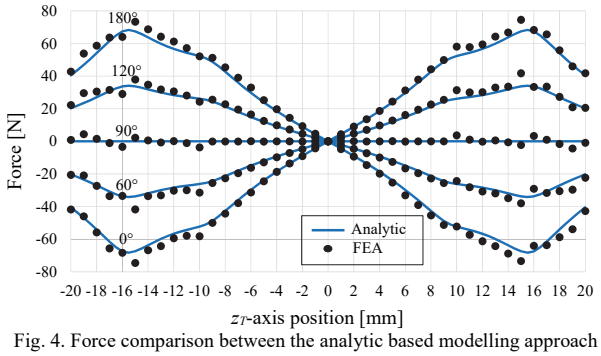

Fig. 4. Force comparison between the analytic based modelling approach and FEA model. The linear region is shown, and it is symmetric. [28]

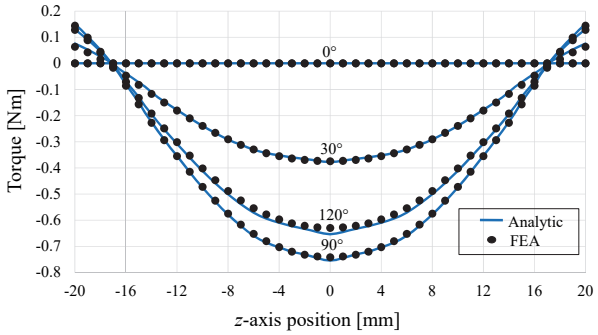

Fig. 5. Torque comparison between the analytic based modelling approach and FEA model. [28]

A. Cylindrical Magnet Separation Length

In the proof-of-principle design the cylindrical tube magnets were vertically separated by a distance, z_{co} = 3.25mm. Fig. 6 shows the change in axial force as a function of z_T for different tube magnet separation lengths, z_{co}. It can be seen that when z_{co} = 0 the peak force is improved by 17% and the linear displacement region is maximized. Therefore, based on this analysis the separation length between the tube magnets was set to z_{co} = 0 for the rest of this analysis. Defining the maximum linear stoke length as

$$z_m = \max(z_T) \tag{5}$$

a the stroke length displacement ratio can be defined as

$$\Gamma_d = \frac{2 \cdot z_m}{h_c} = 1 \tag{6}$$

where h_c = cylindrical tube magnet height.

B. Magnet Height Ratio

A magnet height ratio can be defined as

$$\Gamma_h = \frac{h_r}{h_c} \tag{7}$$

where h_r = rectangular cuboidal height. A plot of the force as a function of translational position, z_T, for different height ratios, Γ_h, is shown in Fig. 7. When the cuboidal height is greater than the cylinder height the linear travel length, z_T, is not extended and the peak force is degraded. Therefore, a magnet relative height ratio Γ_h=1 is recommended.

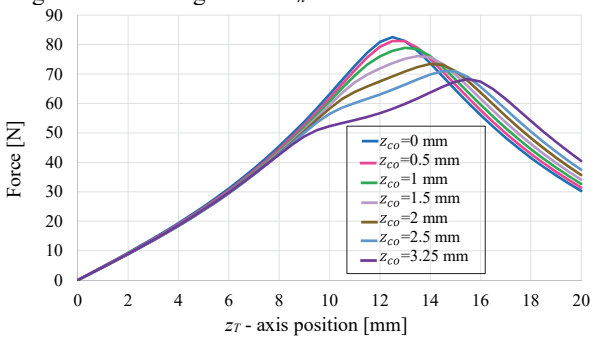

Fig. 6. Force-displacement relationship for different separation lengths, z_{co}, between the two diametric magnetized cylindrical tube magnets.

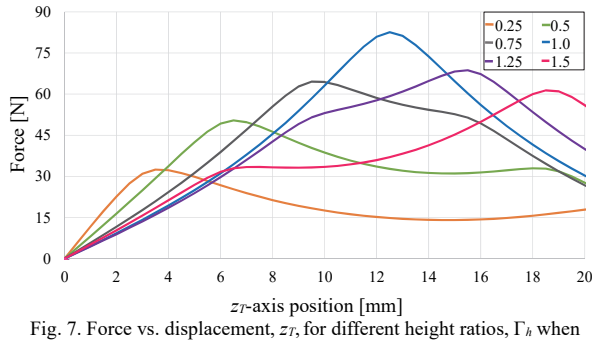

Fig. 7. Force vs. displacement, z_T, for different height ratios, Γ_h when θ_k = 0° and (z_{co},h_c) = (0,25) mm.

C. Height-to-Width Ratio

Keeping the cylinder and cuboidal magnet height ratio equal, Γ_h=1, the cuboidal height-to-width ratio, defined as

$$\Gamma_{hw} = \frac{h_r}{w} \tag{8}$$

was varied for different translational offsets, z_T, the resulting plot is shown in Fig. 8. It can be seen that as Γ_{hw} increases the peak force and translational travel length increases. In Fig. 9 an r^2 correlation coefficient is also shown for each Γ_{hw} plot and this shows that a smaller Γ_{hw} improves the linearity. Interestingly, the relationship between the maximum force and maximum stroke length, z_m is linear, this is shown in Fig. 10. However, when Γ_{hw} increases the peak force increases at a diminishing rate. The force density as a function Γ_{hw} is shown in Fig. 11 and the peak occurs when

$$\Gamma_{hw} = 2\,. \tag{9}$$

D. Depth-to-Width Ratio

A depth-to-width ratio for the cuboidal magnet can be defined as

$$\Gamma_{dw} = \frac{d}{w} \tag{10}$$

A plot of the force as a function of Γ_{dw} and z_T is shown in Fig. 12 for the case when (Γ_h, Γ_{hw}, z_{co}) = (1,2,0) and the cylindrical tube magnet radius was kept fixed at r_o = 6.25 mm. The linearity and force increase as Γ_{dw} increases. Fig. 13 shows the calculated linearity r^2 value for four different cases. Fig. 14 shows that the peak force density occurs at $\Gamma_{dw} \approx 1.0$ but by increasing Γ_{dw} up to Γ_{dw} = 1.2 a higher force can be obtained without a significant force density reduction. Therefore Γ_{dw} = 1.1 was selected.

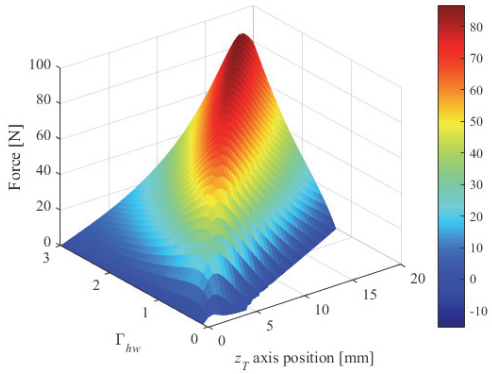

Fig. 8. The force as a function of height-to-width ratio, Γ_{hw}, and axial offset position, z_T, when Γ_h=1 and (z_{co},w,r_o) = (0,12.5,6.25) mm.

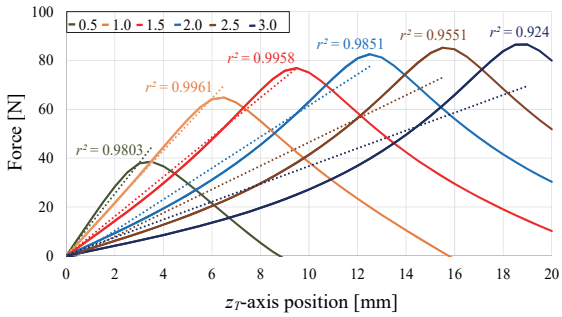

Fig. 9. Force as a function of axial position, z_T for different height-to-width ratio, Γ_{hw}, when h_r=h_w .The r^2 correlation coefficient is also shown it is computed only up to the maximum force value.

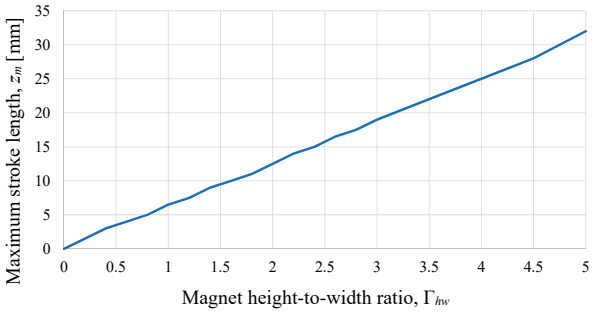

Fig. 10. Maximum linear stoke length z_m , as a function of the height to width ratio, Γ_{hw}.

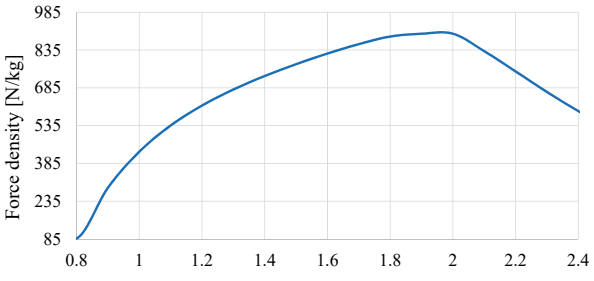

Fig. 11. Force density as a function of the height-to-width ratio.

E. Diameter-to-Width Ratio

The cylindrical tube and cuboidal magnet diameter-to-width ratio can be defined as

$$\Gamma_{2rw} = \frac{2r_o}{w} \tag{11}$$

Keeping (Γ_h, Γ_{hw}, Γ_{dw}, z_{co}) = (1, 2, 1.1, 0) a plot of the force as a function of Γ_{2rw} is shown in Fig. 15. As Γ_{2rw} increases the linearity improves, this is shown in Fig. 16 for five different ratio values, however the force density peaks at

$$\Gamma_{2rw} = 1.2\,. \tag{12}$$

as shown in Fig. 17. Therefore, this value was selected.

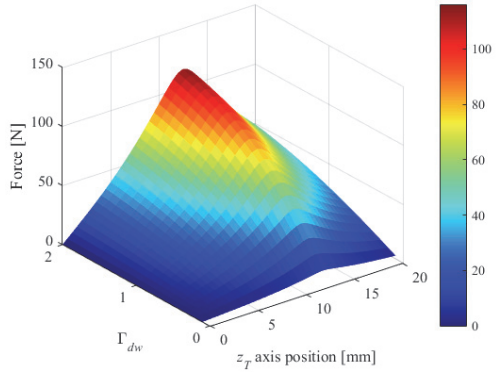

Fig. 12. Plot of the spring force as a function of depth-to-width ratio, Γ_{dw}, and translational displacement, z_T, when θ_k = 0 and (z_{co},h_c,h_r,r_o) = (0, 25, 25, 6.25) mm.

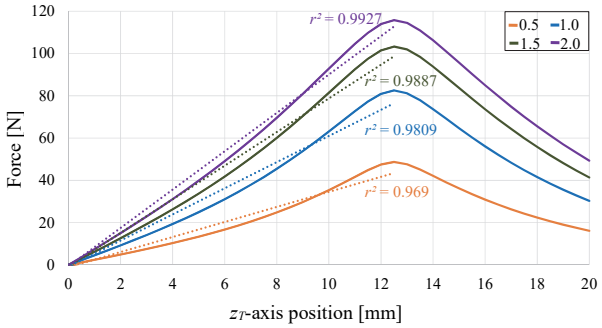

Fig. 13.Force vs. displacement for different cuboidal depth ratios, Γ_{dw}, The r^2 correlation coefficient is also shown.

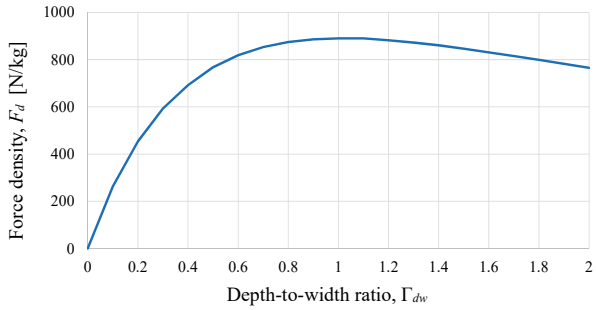

Fig. 14.Force density as a function of the depth-to-width ratio when θ_k = 0 and (z_{co},h_c,h_r,r_o) = (0, 25, 25, 6.25) mm

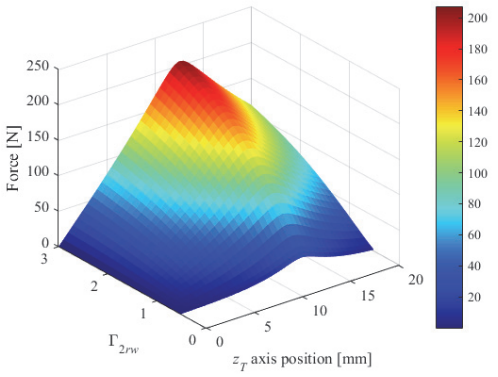

Fig. 15. A plot of the spring force as a function of the diameter-to-width ratio, Γ_{2rw}, and translational displacement, z_T when $(\Gamma_h, \Gamma_{hw}, \Gamma_{dw}, z_{co}) = (1, 2, 1, 0)$ mm

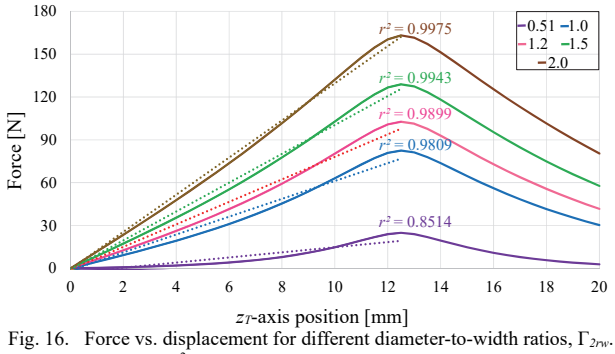

Fig. 16. Force vs. displacement for different diameter-to-width ratios, Γ_{2rw}. The r^2 correlation coefficient is also shown.

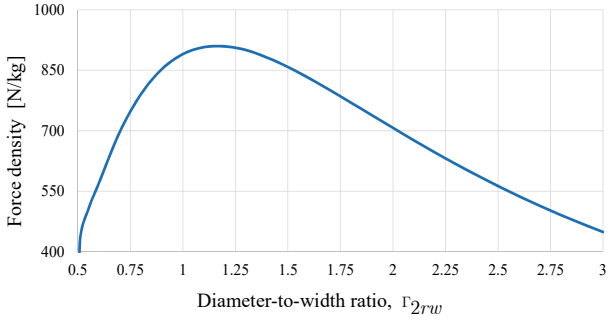

Fig. 17. Force density for different diameter to width ratios.

IV. Design Comparison

Based on the parameter sweep analysis the scaling ratios as stated in Table I are recommended. Using these ratios, the magnet parameters for a stroke length of 12.5mm and 100mm are given in Table II. Table III shows the performance parameters for the 12.5mm stroke length design. Note that for the 100 mm stroke length the airgap was increased to g = 2mm. Using the parameters defined in Table II the force and torque as a function of axial position, z_T, was plotted for the 12.5mm stroke length design. The comparison with the original design is shown Fig. 18, the improved linearity and peak force is evident. The force relationship for the 100mm stroke length design is shown in Fig. 19 it can be seen that a highly linear stroke length can be obtained.

TABLE I
RECOMMENDED SCALING RATIOS

Ratio	Equation	Value
Tube magnet separation	z_{co}	0
Displacement ratio, Γ_d	$2\max(z_T)/h_c$	1
Height ratio, Γ_h	h_r/h_c	1
Height-to-width ratio, Γ_{hw}	h_r/w	1
Depth-to-width ratio, Γ_{dw}	d/w	1.1
Diameter-to-width ratio, Γ_{2rw}	$2r_o/w$	1.2

TABLE II
RECOMMENDED PARAMETER VALUES

Description		Design Equation	Stroke length, z_m [mm]	
			12.5	100
Rectangular cuboidal magnet	Height, h_r	$2 \cdot z_m$	25	200
	Width, w	$w = h_r/2$	12.5	100
	Depth, d	$d = 1.1w$	13.75	110
Cylinder tube magnet	Height, h_c	$h_c = h_r$	25	200
	Outer radius, r_o	r_o=1.2w/2	7.5	60
	Separation length, z_{co}	0	0	0
Airgap, g		-	0.5	2

TABLE III
PERFORMANCE COMPARISON

Design	Original	Recommended	Units
Peak stroke length	10 mm	12.5 mm	
Peak force	52.3	109.5	N
Peak torque	-0.74	-1.0	N·m
Peak energy	0.51	1.27	J
Peak stiffness	5230	8760	N/m
Active volume	12.3	15.8	cm^3
Force density	564 (4230)	922 (6918)	N/kg (kN/m^3)
Torque density	7.9	8.4	N·m/kg
Energy density	5.5 (41.264)	10.7 (80.3)	J/kg (kJ/m^3)

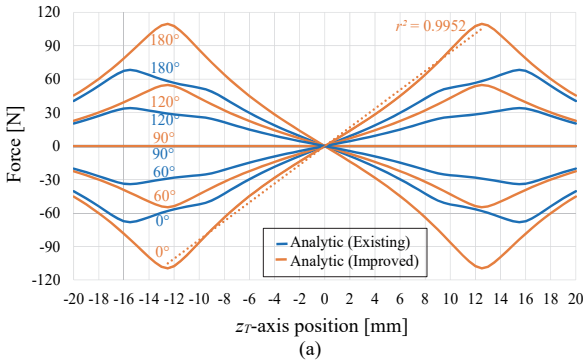

(a)

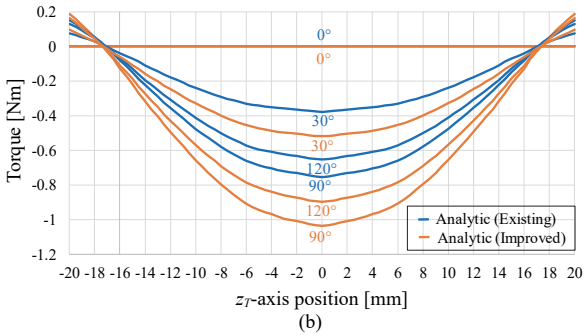

(b)

Fig. 18. (a) Force comparison and (b) torque comparison at different angle adjustment values for the magnetic spring using the existing proof-of-principle geometric values and the recommended design geometry.

V. Energy Density

The energy can be determined for the magnetic springs by computing the work performed by travelling along the stroke length. The work is computed using

$$W(\theta_k) = \int_0^{z_m} F_z(z_T, \theta_k) dz_T \tag{13}$$

where the analytically computed force is derived in [28]. For instance, for the 12.5 mm stroke length design the work done for different angular positions, θ_k, was computed, the simulation result is shown in Fig. 20; the work is a cosinusoidal function. The volumetric energy density can be computed from

$$E_{dv} = \frac{W(0)}{2wdh_r + 2\pi(r_o^2 - r_i^2)h_c} \tag{14}$$

Evaluating (14) gives a peak active region energy density of 80.3 kJ/m^3 (10.7 J/kg) for the 12.5mm stroke length and 95.4 kJ/m^3 (12.7 J/kg) for the 100 mm stroke length design.

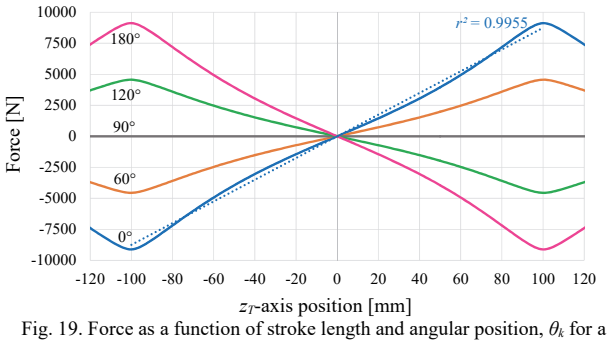

Fig. 19. Force as a function of stroke length and angular position, θ_k for a maximum stroke length of z_m = 100 mm.

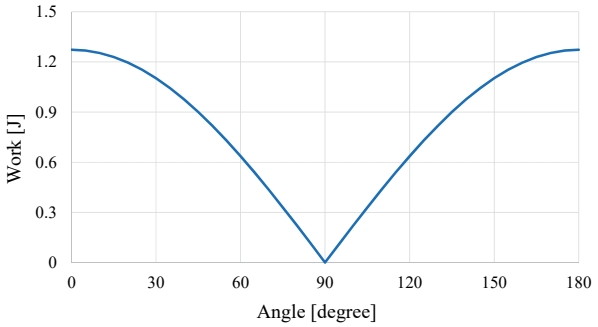

Fig. 20. Work done for different angles of the magnetic spring

VI. Force-Torque Relationships

The force as a function of stroke length for the 12.5mm recommended design is highly linear and can be accurately described by

$$F_z(z_t, \theta_k) = [F_m \cos(\theta_k)] z_t \tag{15}$$

where F_m = 8.7664 N/mm is the peak spring force. The stiffness is defined by the term within the square brackets. When the magnet has a negative stiffness, the spring is in an unstable position. The torque needed to create the desired stiffness values is accurately described by

$$T_z(z_t, \theta_k) = -T_m \sin(\theta_k) \cos(k z_t) \tag{16}$$

where $k = \pi/34$ and T_m = 1.0 N·m peak torque.

VII. Experimental Prototype

At the time of paper submission a proof-of-principle experimental prototype of the adjustable magnetic spring was being assembled. The experimental prototype is shown in Fig. 21, Two mechanical springs have been put in parallel with the adjustable magnetic spring and so when the magnetic spring stiffness is made negative the total spring stiffness is significantly lowered. This then enables the resonance capability of the device to be studied when different low frequency forcing input are applied. The same magnet dimensions as given in Table I have been used.

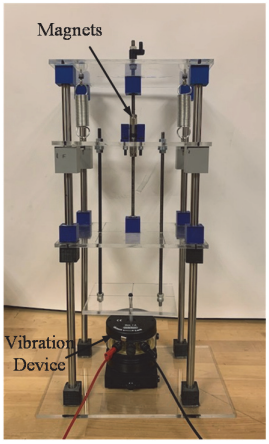

Fig. 21. Magnetic spring experimental setup with a vibration force actuator.

Conclusion

This paper presented the scaling analysis for a new type of variable stiffness magnetic spring. The magnetic spring was shown to exhibits a highly linear stroke length with an adjustable spring constant. Both positive and negative spring stiffness values can be obtained. An analytic based magnetic charge modelling approach was utilized to conduct the sizing analysis and a recommended set of sizing equations for the presented adjustable magnetic spring was presented.

Acknowledgements

The authors would gratefully like to thank the JMAG and Solidworks corporation for the use of their FEA software. This material is based upon work partially supported by the Department of Energy's Office of Energy Efficiency and Renewable Energy (EERE) under the Water Power Technologies Office award number DE-EE0001837.

References

[1] D. G. Wilson, G. Bacelli, R. D. Robinett, U. A. Korde, O. Abdelkhalik, and S. F. Glover, "Order of magnitude power increase from multi-resonance wave energy converters," presented at the OCEANS 2017, Anchorage, 2017.

[2] J. V. Ringwood, G. Bacelli, and F. Fusco, "Energy-maximizing control of wave-energy converters: the development of control system technology to optimize their operation," *IEEE Control Systems Magazine*, vol. 34, no. 5, pp. 30-55, Oct. 2014.

[3] J. K. H. Shek, D. E. Macpherson, M. A. Mueller, and J. Xiang, " Reaction force control of a linear electrical generator for direct drive wave energy conversion," *IET Renewable Power Generation*, vol. 1, no. 1, pp. 17-24, March 2007.

[4] D. B. Stewart and J. S. Gerber, "Active Impedenace matching system and methods for wave energy converter " USA Patent US 7,305,823 B2, 2007.

[5] P. Moller and J. H. Todalshaug, "Tank testing of high-efficiency phase-controlled wave energy converter CorPower Ocean, Infrastructure Access Report," 18 Feb. 2015.
[6] D. Rodriguez-Cianca, M. Weckx, R. Jimenez-Fabian, D. Torricelli, J. Gonzalez-Vargas, M. C. Sanchez-Villamañan*, et al.*, "A variable stiffness actuator module with favorable mass distribution for a bio-inspired biped robot," *Frontiers in Neurorobotics*, vol. 13, no. 20, pp. 1-12, 2019.
[7] G. Tonietti, R. Schiavi, and A. Bicchi, "Design and control of a variable stiffness actuator for safe and fast physical human/robot interaction," in *IEEE Intern. Conf. Robotics Auto.* , Barcelona, Spain, pp. 526-531,2005.
[8] B. Vanderborght, A. Albu-Schaeffer, A. Bicchi, E. Burdet, D. G. Caldwell, R. Carloni*, et al.*, "Variable impedence actuators: a review," *Robotics and Auto. Syst.*, vol. 61, no. pp. 1601-1614, 2013.
[9] H. Huang, G. V. Merrett, and N. M. White, "Design of a linearized magnetic spring for body-worn inertial energy harvesters," in *2012 Ninth International Conference on Networked Sensing*, Antwerp, pp. 1-4,2012.
[10] A. Sudano, D. Accoto, L. Zollo, and E. Guglielmelli:, "Design, Development and Scaling Analysis of a Variable Stiffness Magnetic Torsion Spring," *International Journal of Advanced Robotic Systems*, vol. 10, no., 2013.
[11] R. Olaru, A. Arcire, C. Petrescu, M. M. Mihai, and B. Girtan, "A novel virbration actuator based on active magnetic spring," *Sensors and Actuators A: Physical*, vol. 264, no. pp. 11-17, 2017.
[12] Q. Zhang, Y. Wang, and E. S. Kim, "Electromagnetic energy harvester with flexible coils and magnetic spring for 1–10 Hz resonance," *Jour. Microelectromechanical Sys.*, vol. 24, no. 4, pp. 1193-1206, Aug. 2015.
[13] M. A. Woodward and M. Sitti, "Universal custom complex magnetic spring design methodology," *IEEE Trans. Magn.* , vol. 54,, no. 1, pp. 1-13, Jan. 2018.
[14] W. Robertson, B. Cazzolato, and A. Zander, "A multipole array magnetic spring," *IEEE Trans. Magn.*, vol. 41, no. 10, pp. 3826 - 3828, 2005.
[15] D. T. E. H. v. Casteren, J. J. H. Paulides, J. L. G. Janssen, and E. A. Lomonova, "Analytical force, stiffness, and resonance frequency calculations of a magnetic vibration isolator for a microbalance," *IEEE Trans. Ind. Appl.*, vol. 51, no. 1, pp. 204-210, 2015.
[16] N. Gîrtan and R. Olaru, "Improving the performance of a vibration electromagnetic actuator based on active magnetic springs," in *Intern. Conf. Exp. Electrical Power Eng.*, Lasi, Romania, pp. 284-289,2018.
[17] W. Wu, X. Chen, and Y. Shan, "Analysis and experiment of a vibration isolator using a novel magnetic spring with negative stiffness," *Journal Sound Vibration*, vol. 333, no. pp. 2958-2970, 2014.
[18] R. Olaru, A. Arcire, C. Petrescu, M. M. Mihai, and B. Girtan, "A novel vibration actuator based on active magnetic spring," *Sensors and Actuators A: Physical*, vol. 264, no. pp. 11-17, 2017.
[19] W. Robertson, "Modelling and design of magnetic levitation systems for vibration isolation.," Ph.D., Mech. Engineering, University of Adelaide, 2013.
[20] G. Jungmayr, E. Marth, W. Amrhein, H. Berroth, and F. Jeske, "Analytical stiffness calculation for permanent magnetic bearings with soft magnetic materials," *IEEE Trans. Magn.*, vol. 50, no. 8, p. Art. no. 8300108, 2014.
[21] R. Safaeian and H. Heydari, "Comprehensive comparison of different structures of passive permanent magnet bearings," *IET Electric Power Applications*, vol. 12, no. 2, pp. 179-187, 2018.
[22] S. A. J. Hol, "Design and Optimization of a Magnetic Gravity Compensator " Ph.D. Dissertation Eindhoven: Technische Universiteit 2004.
[23] P. J. Patt, M. Kisco, and F. R. Stolfi, "Linear magnetic spring and spring/motor combination " USA Patent 5,017,819, 1989.
[24] J. L. G. Janssen, J. J. H. Paulides, E. A. Lomonova, B. Delinchant, and J.-P. Yonnet, "Design study on a magnetic gravity compensator with unequal magnet arrays," *Mechatronics*, vol. 23, no. pp. 197-203, 2013.
[25] B. E. Paden, C. Chen, and O. J. Fiske, "Magnetic spring and actuators with multiple equilibrium position," 7,265,470 B1, 2009.
[26] Y.Zheng, X. Zhang, S. Xie, and Y. Zhang, "Theoretical and experimental study of a vibration isolator using a negative stiffnes magnetic spring " presented at the 24th Inter. Cong. Sound and Vibration, London, 23-27, 2017.
[27] W. S. P. Robertson, "Modelling and Design of Magnetic Levitation Systems for Vibration Isolation " Ph.D. Dissertation, Mech. Engineering, The Univ. Adelaide, 2013.
[28] M. E. Hossain and J. Z. Bird, "Studying a variable stiffness magnetic actuator using a magnetic charge integral approach," *Submitted to IEEE Trans. Magn.*, no., 2019.
[29] O. D. Jefimenko, *Electricity and Magnetism*. New York: Meredith Publishing Co., 1966.